Auxiliary alkyl chain modulated spin crossover behaviour in $[Fe(H_2Bpz_2)_2(C_n\text{-bipy})]$ complexes

Yunnan Guo[a,b], Aurelian Rotaru[c], Helge Müller-Bunz[d], Grace G. Morgan[d], Shishen Zhang[a], Shufang Xue[*,a,b] and Yann Garcia[*,b]

ABSTRACT: Three new alkyl chain substituted complexes $[Fe(H_2Bpz_2)_2(C_n\text{-bipy})]$ (pz = pyrazolyl, C_n-bipy = bipyridine alkyl chain diester, n = 3 (**3**), 4 (**4**) and 5 (**5**)) show versatile spin state switching behaviour with different "tail" length as revealed by structural and magnetic analysis. The most striking phenomenon is observed for **5** which undergoes an abrupt spin transition accompanied by thermal hysteresis of ca. 10 K, which is attributed to crystal packing effects derived from the competition between π···π and C-H···O interactions. Interestingly, each of the complexes exhibits similar gradual and complete spin crossover in methanol solution with a transition temperature around 249 K, as deduced from temperature-dependent UV-vis spectroscopy. This highlights the differences between solid state (ligand field; crystal packing) and solution (ligand field; solvation) effects on spin crossover. This work demonstrates that the length of the complex's alkyl chain substituents on the complex can have a large impact on the transition temperature and profile of solid state spin crossover, offering a potential path to the fabrication of soft matter spin crossover materials.

a. Department of Chemistry, Key Laboratory of Surface & Interface Science of Polymer Materials of Zhejiang Province, Zhejiang Sci-Tech University, Hangzhou 310018, China. E-mail: sfxue@zstu.edu.cn;

b. Institute of Condensed Matter and Nanosciences, Molecular Chemistry, Materials and Catalysis (IMCN/MOST), Université catholique de Louvain, Place L. Pasteur 1, Louvain-la-Neuve 1348, Belgium. E-mail: yann.garcia@uclouvain.be;

c. Department of Electrical Engineering and Computer Science & MANSiD Research Center, "Stefan cel Mare" University, University Street, 13, Suceava 720229 Romania;

d. School of Chemistry, University College Dublin, Belfield, Dublin 4, Ireland.

† Electronic supplementary information (ESI) available. For ESI and crystallographic data in CIF or other electronic format see DOI:

1. Introduction

Spin crossover (SCO) materials continue to generate research interest from both fundamental and applied disciplines.[1] The magnetic modification between high-spin (HS) and low-spin (LS) states can be modulated in a reversible, detectable and controllable fashion by the action of

external stimuli.[2-5] This is usually accompanied by drastic changes in the magnetic moment, optical properties (colour) or dielectric constants with potential applications in data storage, molecular electronics, sensors and molecular switches.[6, 7] Ideally, for a practical application, the properties referring to an abrupt and complete signal response with a hysteresis, if sufficiently wide, confers to the material an exploitable memory function.[8] In the solid state, the design of superior SCO materials depends on both ligand field strength and cooperative effects. It is recognized that the transition temperature ($T_{1/2}$) is primarily governed by the ligand field strength evaluated by a series of crystal structures indexes[9, 10]. Stronger metal-ligand bonding usually results in the LS form of the metal ion because of the lower number of antibonding e_g* electrons producing a less deformable coordination sphere. Hence LS complexes of any metal ion generally adopt more regular coordination geometries than their HS counterparts.[9] In view of cooperative effects, it mainly results from the efficient communication between spin centres in the crystal lattice. Great efforts have been dedicated to enhancing the cooperativity through a 'covalent coordination strategy' in polynuclear complexes[11, 12] or extended frameworks[13], as well as by a 'supramolecular strategy'[14-16] by virtue of elastic contacts involving hydrogen bonding (HB), halogen bonding (XB), π···π interactions and hydrophobic interchain interactions. However, the investigation of SCO behaviour associated with cooperative effects has so far been mainly in the realm of rigid systems, while investigations in soft systems incorporating flexible molecular units remain limited[17]. One typical representative of SCO-soft metal complexes is constructed by introducing long alkyl chains (C_nH_{2n+1}) onto the periphery of the organic ligand skeleton of coordination complexes[8, 18-23], some of which feature an odd-even effect on $T_{1/2}$ as well as an unprecedented melting-triggered reverse HS to LS transition.[8, 24]

Since the well-known SCO complex [Fe(H_2Bpz_2)$_2$(**bipy**)] (**bipy** = bipyridine) was reported in 1997[25], great efforts have concentrated on the investigation of its switchable ability under physical stimuli[26, 27] as well as its real world application immobilised onto a solid support.[28-32] Comparable interests also focus on the modification of bipy[31, 33-36] or pz motif,[37,38] such as by introduction of electron-withdrawing groups,[34, 35] electrons-donating[39] or hydrophilic alkyl tails[33] to fine-tune SCO behaviour. The exact nature of SCO event is dependent on (a) the position of substituents on the bipy group, (b) the electronic effect of substituent as well as (c) crystal packing effects. Among them, our group previously reported two complexes [Fe(H_2Bpz_2)$_2$(**C_1-bipy**)] (**1**) and [Fe(H_2Bpz_2)$_2$(**C_2-bipy**)] (**2**) featuring a distinct SCO due to crystal packing effect and structure disorder of the pz ligand, where **C_1-bipy** and **C_2-bipy** are

dimethyl-2,2'-bipyridyl-5,5'-dicarboxylate and diethyl-2,2'-bipyridyl-5,5'-dicarboxylate, respectively.[35] Of particular relevance to the present study is the modification of SCO behaviour by increasing the 'tail' length of bipyridine diesters. In a crystal engineering approach, we aim to study the influence of these alkyl ester substituents as a structure determining element on the packing of the complexes in the crystal and therefore on the SCO behaviour. Here we present a report on a systematic study of SCO features within three alkyl ester substituted complexes [Fe(H_2Bpz_2)$_2$(**C_n-bipy**)] (n = 3 (**3**), n = 4 (**4**) and n = 5 (**5**)). In the solid state of **3-5**, SCO behaviours are different from complex to complex due to crystal packing effect derived from the competition between π···π and C-H···O interactions. All of them exhibit however gradual and complete SCO in methanol solution with $T_{1/2}$ ~ 249 K as deduced from temperature-dependent UV-vis spectroscopy, a behaviour which is unaffected by the alkyl chain substituents.

2. Experimental section

Syntheses. All chemicals were used as commercially obtained without further purification.

Synthesis of bipyridine diesters. Dipropyl-2,2'-bipyridyl-5,5'-dicarboxylate (**C_3-bipy**), Dibutyl-2,2'-bipyridyl-5,5'-dicarboxylate (**C_4-bipy**) and dipentyl-2,2'-bipyridine-5,5'-dicarboxylate (**C_5-bipy**) were prepared using literature procedures[40].

Synthesis of complexes 3-5: Syntheses were performed under $Ar_{(g)}$ using Schlenk techniques. Fe(H_2Bpz_2)$_2$(**C_3-bipy**) (**3**). To a solution of K[$H_2B(pz)_2$] (44 mg, 0.24 mmol) in methanol (2 mL) was added a solution of Fe(ClO_4)$_2$·6H_2O (44 mg, 0.12 mmol) in methanol (2 mL). The formed $KClO_4$ precipitate was removed by filtration, affording a yellow solution. A solution of **C_3-bipy** (39 mg, 0.12 mmol) in dichloromethane (4 mL) was then added dropwise to the solution, causing an immediate colour change to green. After the solution was stirred for 2 h at room temperature, subsequently, the solution was evaporated using a N_2 gas flow over several days. Needle shaped crystals were obtained (53 mg, 65%). Anal. Calcd. (Found) for **3** ($C_{30}H_{36}N_{10}O_4B_2Fe$): C, 53.13 (52.46); H, 5.35 (5.25); N, 20.65 (20.03). MS (FTMS+pESI): *m*/*z*: 678.25 [M^+].

Fe(H_2Bpz_2)$_2$(**C_4-bipy**) (**4**). The same method as for **3** was followed using **C_4-bipy** (43 mg, 0.12 mmol), which yielded olive-green needle crystals of **4**. Yield: 59 mg (70%). Anal. Calcd. (Found) for **4** ($C_{32}H_{40}N_{10}O_4B_2Fe$): C, 54.43 (53.06); H, 5.71 (5.65); N, 19.83 (18.73). MS (FTMS+pESI): *m*/*z*: 706.28 [M^+].

Fe(H_2Bpz_2)$_2$(**C_5-bipy**) (**5**). The same method as for **3** was followed using **C_5-bipy** (46 mg, 0.12 mmol), which yielded olive-green needle crystals of **5**. Yield: 53 mg (60%). Anal. Calcd for **5**

($C_{34}H_{44}N_{10}O_4B_2Fe$): C, 55.62 (51.73); H, 6.04 (5.53); N, 19.08 (18.71). MS (FTMS+pESI): *m*/*z*: 734.26 [M^+].

Characterization Techniques. Elemental analysis for C, H, and N were performed at Medac Ltd (UK). NMR spectra were recorded at room temperature with a Bruker Avance II 300 MHz instrument. Mass spectra (MS) were recorded on a Q-Exactive spectrometer from ThermoFisher. Infrared spectra (Fig. S1) were recorded on a Shimadzu FTIR-8400S spectrometer with KBr pellets. Magnetic susceptibilities were measured on a Quantum design MPMS-5s SQUID magnetometer. Magnetic data were corrected for the sample holder and diamagnetic contributions. The crystal sample was quickly loaded into a gelatin capsule and immediately inserted within the SQUID cavity. UV-vis spectroscopic measurements were recorded with a UT6A UV-vis spectrophotometer. For temperature-dependent UV-vis spectroscopic measurements, a Cambridge-cryostat with liquid nitrogen and a TIC-304 MA temperature controller from CryoVac were used. The concentration of samples was uniformed as 10^{-3} M. The $\gamma_{HS}(T)$ was calculated from the peak at λ = 670 nm of the MLCT band of the measured absorption spectra by the following two equations[41]:

$$\gamma_{\mathrm{HS}} = \frac{\varepsilon - \varepsilon_{\mathrm{LS}}}{\varepsilon_{\mathrm{HS}} - \varepsilon_{\mathrm{LS}}} \quad (1)$$

$$\varepsilon = \varepsilon_{LS} + \left(\frac{1}{1 + \mathrm{e}^{\Delta H/RT - \Delta S/R}} \right) \left(\varepsilon_{\mathrm{HS}} - \varepsilon_{\mathrm{LS}} \right) \quad (2)$$

Crystallographic data at 100K for complex **5** were collected on a MAR345 image plate using Cu-K_α radiation (λ = 1.54184Å), all other datasets on an Agilent SuperNova with an Atlas CCD Detector using Cu-K_α radiation (λ = 1.54184Å). The crystals were selected, mounted in inert oil and transferred to the cold gas stream for flash cooling. Data were integrated by CrysalisAlisPro (Agilent Technologies (2014), Agilent Technologies UK Ltd., Oxford, UK, Xcalibur/SuperNova CCD system, CrysAlisPro Software system, Version 1.171.38.41) and Bruker FRAMBO. Absorption correction was applied using the integrated multi-scan absorption algorithm. The structures were solved by direct methods (SHELXS) and refined by full-matrix least-squares on F^2 using SHELXL201[42]. The location of the Fe atom was easily determined, and O, N, and C atoms were subsequently located in the difference Fourier maps. The non-hydrogen atoms were refined anisotropically. The H atoms were introduced in calculated positions and refined with fixed geometry with respect to their carrier atoms. CCDC 2086383 (**4**_100 K), 2086384 (**4**_293 K), 2086382 (**5**_100 K) and 2086385 (**5**_130 K) are the supplementary crystallographic data for this paper. They can be obtained free of charge from

the Cambridge Crystallographic Data Center via www.ccdc.cam.ac.uk/data_request/cif.

Table 1. Crystal data and structure refinement for **4** and **5**

Complex	**4**		**5**	
Empirical formula	$C_{32}H_{40}B_2N_{10}O_4Fe$		$C_{34}H_{44}B_2N_{10}O_4Fe$	
Formula weight	706.21	706.21	734.26	734.26
Temperature/ K	100(2)	293(2)	100(2)	130(2)
Crystal system	Monoclinic	Monoclinic	Monoclinic	Monoclinic
Space group	*C*2/*c*	*C*2/*c*	*C*2/*c*	*C*2/*c*
a/Å	29.3326(3)	29.8345(4)	30.2819(3)	30.8770(3)
b/Å	14.4529(2)	14.6697(2)	14.2215(2)	14.3754(1)
c/Å	16.4410(2	17.0434(2)	16.6969(2)	16.9723(2)
α/°	90	90	90	90
β/°	98.9041(8)	100.761(1)	97.2920(10)	100.7263(7)
γ/°	90	90	90	90
V/Å^3	6886.02(15)	7328.09(17)	7132.43(15)	7401.85(13)
Z	8	8	8	8
ρ_{calc}/mg·m^{-3}	1.367	1.280	1.368	1.318
μ/mm^{-1}	3.944	3.704	3.826	3.687
F(000)	2971	2960	3088	3088
Reflections collected	41427	42680	21171	42784
Independent reflections	7230	7690	7199	7769
R_{int}	0.0326	0.0231	0.0402	0.0425
Final *R* indices [*I*>2sigma(*I*)]	R_1 = 0.0362 wR_2 = 0.0966	R_1 = 0.0459 wR_2 = 0.1402	R_1 = 0.0582 wR_2 = 0.1611	R_1 = 0.0335 wR_2 = 0.0851
R indices (all data)	R_1 = 0.0377 wR_2 = 0.0981	$R1$ = 0.0501 $wR2$ = 0.1476	R_1 = 0.0679 wR_2 = 0.1724	R_1 = 0.0388 wR_2 = 0.0894
GOF	1.053	1.059	1.087	1.036
Largest diff. peak and hole/ e·Å^{-3}	0.431 and -0.441	0.56 and -0.37	0.78 and -0.52	0.409 and -0.311

3. Results and discussion

Crystal Structures. Many attempts and various techniques were used to grow single crystals suitable for the structural characterization of complexes **3-5**. Finally, crystalline nature of complex **3** was revealed by a powder X-ray diffraction pattern (Fig. S2), while single crystals suitable for X-ray diffraction were obtained for [Fe(H_2Bpz_2)$_2$(**C_4-bipy**)] (**4**), and [Fe(H_2Bpz_2)$_2$(**C_5-bipy**)] (**5**) following slow evaporation in methanol/dichloromethane mixture under $Ar_{(g)}$ using a Schlenk tube within three days. The crystal structures of **4** and **5** were

determined at the most interesting temperatures of the magnetic measurement. Details of the structure solution and refinement are summarized in Table 1 and selected bond distances and bond angles are listed in Table S1.

Both complexes crystallize in the monoclinic *C*2/*c* space group without any structural phase transition in the detected temperature range. As depicted in Fig. 1, the molecular structures (except terminal alkyl chains) and crystal packing are quite similar to each other. In each complex, the central Fe^{II} is surrounded by one bidentate bipyridine diester group and two $(H_2Bpz_2)^-$ anions affording a N_6 octahedral coordination configuration. The continuous shape measure (CShM) values[43] calculated using SHAPE 2.0 relative to an ideal octahedron, increase slightly from 7.452 (100 K) to 7.944 (293 K) for **4**, while they increase remarkably from 7.973 at 100 K to 8.843 at 130 K for **5**. These values are consistent with a large distortion from an ideal octahedron of the local Fe^{II} geometry for all structures. The same conclusion can be drawn by inspecting the distortion index Σ (the sum of the deviation from 90° of the 12 *cis*-N-Fe-N angles). The Σ values for **4** vary in the range of 44.63-64.12° with $|\Delta\Sigma|$ of 19.49° (from 100 to 293 K) and for **5**, the Σ values increase with $|\Delta\Sigma|$ of 18.35° (heating from 100 to 130 K), reflecting a large structural distortion during the spin transition.

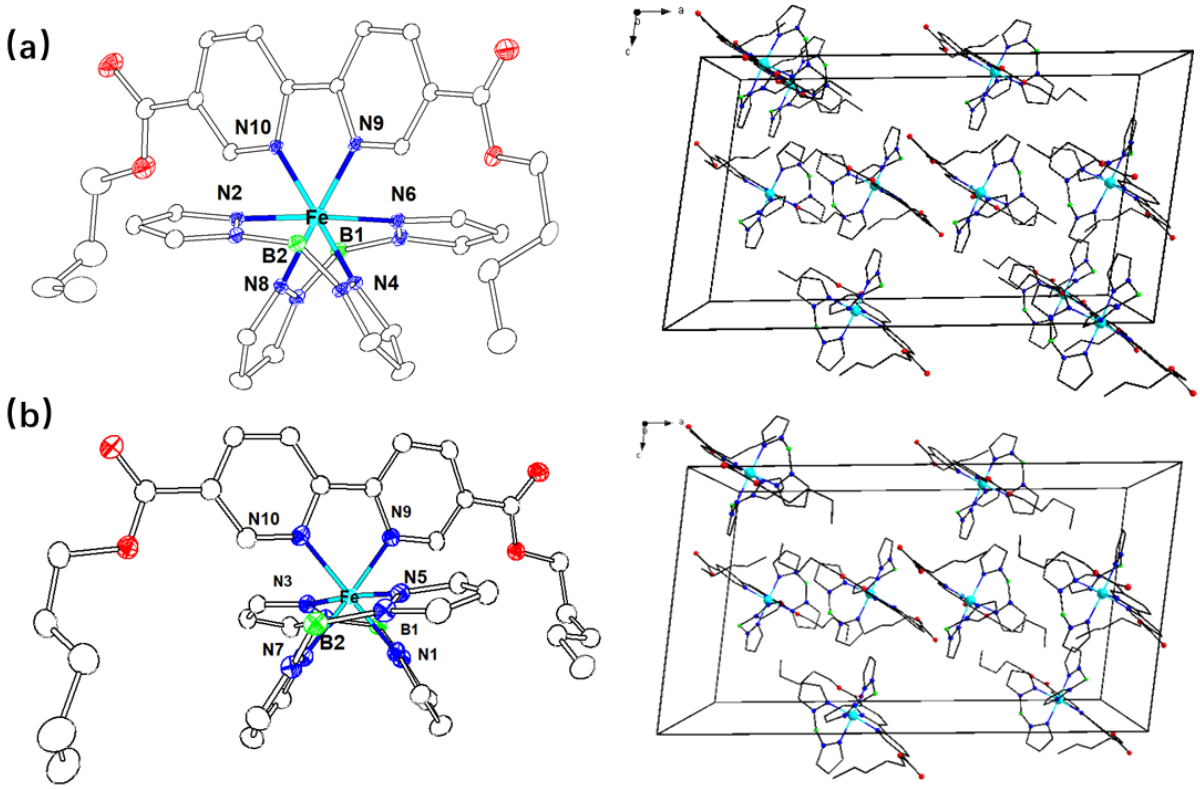

Fig. 1 Molecular structures of complex (left) and packing motifs (right) for (a) **4** and (b) **5** measured at 100 K. Selected atomic numbering is also shown. Hydrogen atoms are omitted. Thermal ellipsoids are drawn at the 50% probability level. Hydrogen and anions are omitted for clarity. Colour code: white (C), blue (N), red (O), green (B) and cyan (Fe^{II}).

In **4**, the two $H_2Bpz_2^-$ anions coordinate *via* the pyrazolyl nitrogen atoms (N2, N4, N6 and N8) and the C_4-bipy ligand coordinates through the N9 and N10 atoms. The *trans*-N-Fe-N angles are in the range of 173.63(5)-175.90(5)° at 100 K. When the two structures at detected temperatures are compared by the overlay, it can be observed that the central moiety does not change much (Fig. 2a). The most obvious difference is in the bond length related to the Fe^{II} ion. The average Fe-N bond lengths are 1.9943 and 2.1890 Å at 100 and 293 K, respectively, which are typical values for an Fe^{II} ion undergoing a LS to HS spin transition. On the basis of available structural data for $Fe^{II}N_6$ analogues[34, 35], we find that the temperature-dependent variation of Fe-N_{bipy} bond distances ($\Delta d_{Fe\text{-}N}$ = 0.255-0.256 Å) is larger than that for the Fe-N_{pz} bond distances ($\Delta d_{Fe\text{-}N}$ = 0.141-0.192 Å). Therefore, the change in Fe-N_{bipy} bond distances may be used as an indicator for spin state determination.

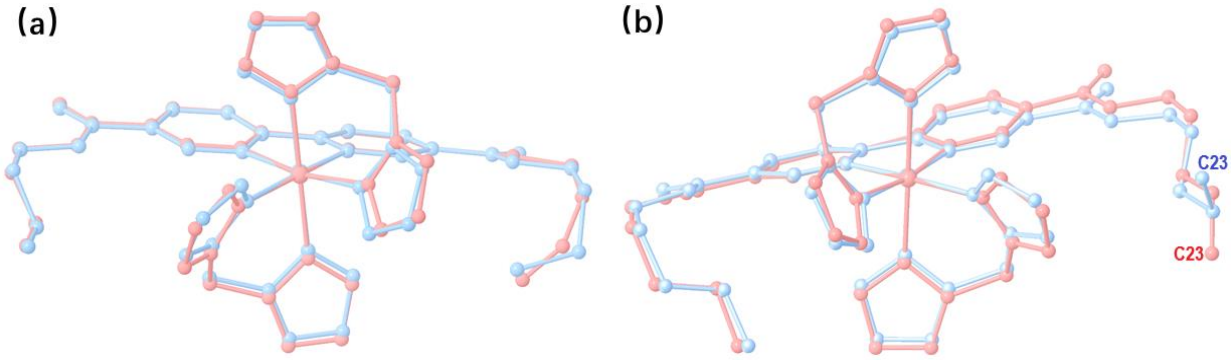

Fig. 2 Overlay of the LS (blue) and HS (red) structures of **4** (a) and **5** (b). Hydrogen atoms mitted for clarity. Structures were overlaid using the atomic coordinates of the FeN_6 cores in Olex2.

The clearest aspect in the molecular structure of complex **5** is also a distortion of the octahedral coordination environment completed by two nitrogen atoms (N9 and N10) as well as four nitrogen atoms (N1, N3, N5 and N7), as described by the *trans*-N-Fe-N angle of 174.09(10)-176.12(10)° and Fe-N distances of 1.977(2)-2.024(2) Å at 100 K. Similar to **4**, complex **5** exhibited dramatic changes in the coordination environment of the Fe^{II} ion as a function of temperature, as witnessed by a larger increase of Fe-N_{bipy} distances (0.25 Å) as compared to Fe-N_{pz} distances (0.17 Å) after the spin transition which may be mainly accounted for by the fact that the bipy-type ligand acts as a better π-electron acceptor than pyrazolyl ligands[35]. Besides, one arm of the alkyl chain displayed a peculiar rotational motion of C22-C23 with a rotation angle of 119.10° (Fig. 2), which may influence the supramolecular interaction.

Solid-state Magnetic Properties. The magnetic susceptibilities of **3-5** were measured on a SQUID magnetometer, and all of the samples investigated here displayed clear SCO but with distinct thermal evolution as shown in Fig. 3 in the form of $\chi_M T$ *vs.* T plots, where χ_M is the molar magnetic susceptibility and T is the temperature. The $\chi_M T$ value of **3-5** at 300 K is around

3.53-3.59 $cm^3mol^{-1}K$, lying in the range typically observed for Fe^{II} ions in the HS ($S = 2$) states[3].

The SCO profile of complex **3** is gradual, $\chi_M T$ value exhibits a nearly constant evolution at 3.59 $cm^3mol^{-1}K$ in the temperature range of 300-210 K, after which it decreases gradually, disclosing a HS → LS conversion and then reaching a second plateau at 1.17 $cm^3mol^{-1}K$ over the range of 30-80 K, indicative of a nearly half-spin transition. Complex **4** exhibits a gradual and complete SCO behaviour. Indeed, the thermal evolution of $\chi_M T$ continuously decreases from 300 to 170 K, and then reaches 0.04 $cm^3mol^{-1}K$ at 10 K. The SCO profile can be fitted well using the ideal solution model[44] (Fig. S3), leading to a $T_{1/2}$ of 172.5(1) K, an enthalpy ΔH_{HL} of 20.01(2) kJ mol^{-1}, and an entropy ΔS_{HL} of 58.4(5) J K^{-1} mol^{-1}. The $\chi_M T$ product of **5** is 3.57 $cm^3mol^{-1}K$ at 300 K and remains almost constant upon cooling to 130 K. Upon further cooling, the $\chi_M T$ value drops abruptly to 0.2 $cm^3mol^{-1}K$ at 110 K. This behaviour indicates a complete one-step SCO from a HS to a LS state. The measurement performed in the subsequent heating mode revealed the presence of a 10 K thermal hysteresis. The transition temperature are $T_c^{\downarrow}$ = 123 K and $T_c^{\uparrow}$ = 133 K in the cooling and warming modes, respectively. Therefore, not only the spin transition temperatures but also the character of SCO can be effectively adjusted by the length of alkyl chain.

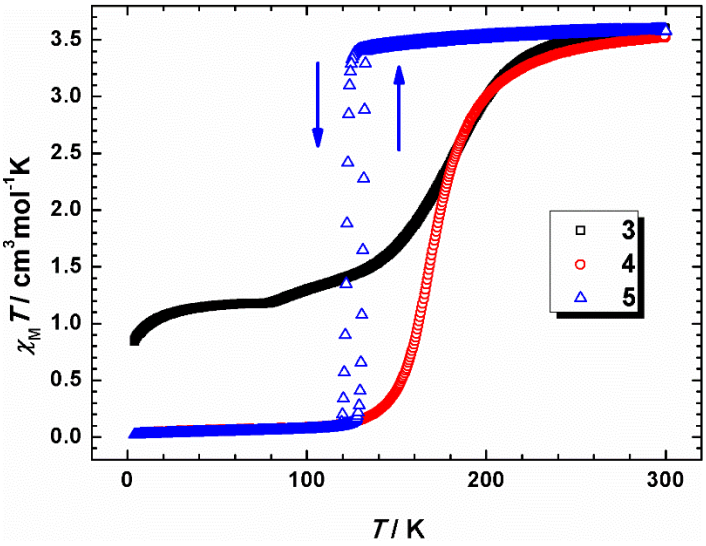

Fig. 3 Temperature dependence of the $\chi_M T$ product for **3**-**5**.

Magneto−Structural Correlation. Modulation of the SCO profile in such prototype [Fe(H_2Bpz_2)$_2$(bipy)] complexes is mainly ascribed to the combination of electronic substituent effects on the bipy ligand,[34] C-H···O supramolecular interactions involving the terminal ester group as well as structural disorder of the pyrazolyl ligand.[35] In cases of **4** and **5**, it can be shown that the distinct SCO properties are intrinsic to the crystal packing effect of the materials as there is no structure disorder during the spin transition and both complexes share the same π-

acceptor properties of the ester series as revealed by the calculation of energy difference (Δ) between the highest d_π orbital and the d_{z^2} orbital.[35]

As far as the structure-property relationship is concerned, careful inspection of the structures provides some clues. At first glance, the $T_{1/2}$ values of **5** are shifted to lower temperatures. By considering the molecular structural aspect, **5** possesses the longer Fe-N_{av} distance (2.000 Å) and smaller *cis*-N-Fe-N angle (90.045°) at 100 K than those in **4** (1.994 Å and 90.061°, Table S1†), which provide a smaller ligand field and tend to decrease the $T_{1/2}$ value. This is also confirmed by the larger CShMs value of **5** (7.973) compared with that of **4** (7.452) at 100 K suggesting that large distortion of the Fe^{II} octahedron favours the HS state. Consideration of the supramolecular interactions, detailed in Fig. 4 and Table S2, shows that there are offset face-to-face π···π interactions (type A) involved with the bipy-type ligands and edge-to-face C-H···π hydrophobic interchain interactions (type B) derived from the bipy-type ligand and pyrazolyl ring between the nearest neighbouring complex units. At 100 K, crystal packing structure of **4** shows that the nearest two complex units form rather weaker intermolecular π···π and C-H···π interactions than those in **5** as evidenced by the larger distances observed in **4** (type A: 3.347 Å; type B: 3.348 Å) compared to **5** (type A: 3.330 Å; type B: 3.338 Å). Therefore, the nearest separation of Fe···Fe within the π···π coupled dimers is 7.6788(8)·and 7.6512(8) Å for **4** and **5**, respectively, which suggests more loose packing exist in **4**. It is indicative that π···π interactions in **5** are significant to account for the increase of the cooperativity. Further to this, two types of intermolecular C-H···O interactions linking pairs of complex units to form a 1D supramolecular structure were identified: one involves the ester oxygen atom connecting the pyrazolyl ring of an adjacent molecules (for **4**, C2(H2)···O2[a] = 3.5305(2) Å and for **5**, C8(H8)···O2[b] = 3.5762(4) Å, symmetry code: [a], *x*, *-y*, -0.5+*z;* [b], *x*, 1-*y*, 0.5+*z*); the other occurs with the carbonyl group and the terminal alkyl carbon atom (for **4**, C33(H33A)···O3[c] = 3.3023(15) Å and for **5**, C33(H33)···O3[d] = 3.3561(4) Å, symmetry code: [c], *-x*, *y*, 0.5-*z;* [d], 1-*x*, 1-*y*, 2-*z*). In this regard, the shortest Fe···Fe distance between adjacent pair is 8.8075(5) and 8.8722(7) Å for **4** and **5**, respectively, reflecting stronger C-H···O interactions in **4** compared with **5**. As a result, competition between above two type supramolecular interactions is responsible for the larger cooperative effects observed in **5** with 10 K hysteresis and sharp spin transition.

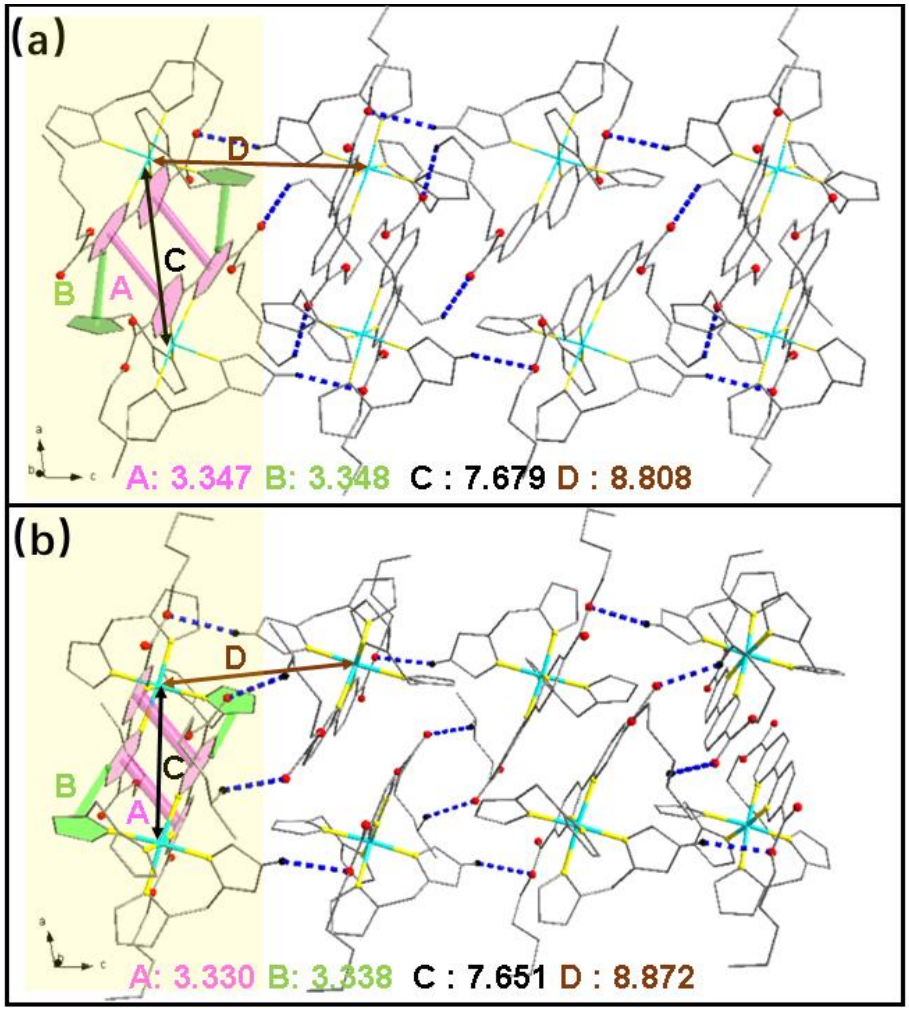

Fig. 4 Illustration of the intermolecular π···π interactions (A, pink), C-H···π interactions (B, green) as well as C-H···O HBs (blue dashed line) in **4** (a) and **5** (b).

Solution-State Magnetic Studies. In order to determine the evolution of the spin state behaviour in the absence of crystal-packing effects, temperature-dependent ultraviolet-visible light (UV-vis) spectra in methanol were undertaken in the range of λ = 300-1000 nm. Lower temperature measurements are limited by the freezing point of methanol (175.2 K). As shown in Fig. 5, in the visible region, metal-to-ligand charge transfer (MLCT) bands from the metal d_π orbitals into π^* orbitals of the ligands[28] at 300 K (HS) evolve to a more intense three-band pattern centred at λ = 410, 610 and 670 nm at 175 K (LS; Fig. 5), indicating the occurrence of thermal SCO as observed in other analogous complexes.[28, 36-38] As the intensity of the MLCT band differs in the HS and LS state, it can be taken to monitor the spin transition. From the temperature-dependent MLCT band at λ = 670 nm (Fig. 5, inset), the relative HS fraction γ_{HS} can be derived as a function of temperature by applying eq 1 and 2, which affords the thermodynamic parameters of the SCO listed in Table 2 and the plot of γ_{HS} *vs.* T reproduced in Fig. 6. Although there are small variations in the enthalpy and entropies of these equilibria, the transition temperatures of the complexes are close to each other indicative of comparable ligand

field strengths around the Fe^{II} centres. In contrast to the thermal evolution in the solid state, each complex undergoes typical gradual SCO equilibria in solution with $T_{1/2}$ around 249 K (Fig. 6), as a result of weaker cooperative effects in the solution, and the quenching of intermolecular interactions in solution.[37]

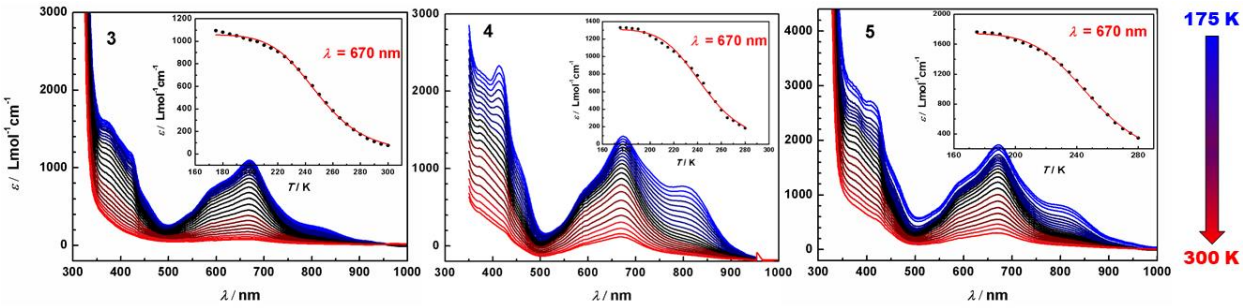

Fig. 5 VT UV/vis spectra of **3**-**5** at 175-300 K in methanol. Inset: transformation of absorption maximum at λ = 670 nm over the same temperature range with a cooling step of 5 K.

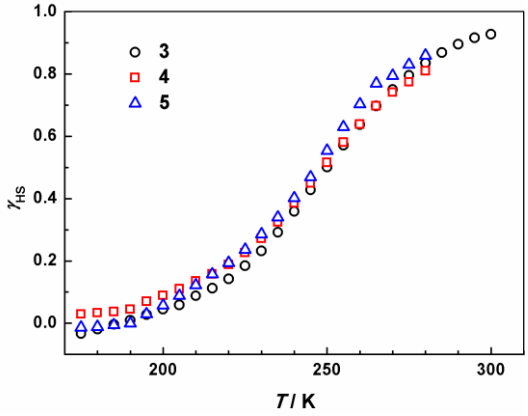

Fig. 6 Evolution of the HS molar fraction *vs.* temperature calculated *via* the UV-vis method for **3**-**5**.

Table 2. Overview of thermodynamic parameters ΔH, ΔS and $T_{1/2}$ for the gradual SCO of **3**-**5** in methanol[a]

Complex	ΔH / kJ mol^{-1}	ΔS / J mol^{-1}K^{-1}	$T_{1/2}$[b] / K	ε_{HS} / Lmol^{-1}cm^{-1}	ε_{LS} / Lmol^{-1}cm^{-1}
3	29.5(11)	118(4)	249.2	0	1059(6)
4	28.0(17)	112(5)	248.9	0	1312(13)
5	26.5(9)	106(2)	249.8	0	1746(9)

[a] Results were obtained by fitting eq 2 to experimental data; [b] with $\Delta H = T_{1/2}\Delta S$.

4. Conclusions

Here we have introduced three new alkyl chain substituted iron(II) complexes $[Fe(H_2Bpz_2)_2(C_n\text{-bipy})]$ (n = 3 (**3**), n = 4 (**4**) and n = 5 (**5**)) displaying various spin state switching behaviours. With regard to their magnetic properties in the solid state, complex **3** displays a gradual and incomplete SCO whereas **4** and **5** feature completely gradual and abrupt spin transitions, respectively. Moreover, it is found that the transition temperatures and SCO profiles, such as abruptness and hysteresis, were obviously changed due to cooperativity derived from the competition between π···π stacking and C-H···O interactions. Variable-

temperature UV-vis studies of **3**-**5** in methanol solution show that the transition becomes gradual with $T_{1/2}$ around 249 K. This mirrors differences between solid state (ligand field; crystal packing) and solution (ligand field; solvation) effects on spin crossover. This work provides new insights for the fabrication of SCO-active complexes based soft materials, offering a potential path to the development of advanced functional devices in the future.

Conflicts of interest

There are no conflicts to declare.

Acknowledgements

This research was supported by FNRS (CR 28109061, CR 24918505, CDR 33694457, PDR T.0095.21), the initial founding of Zhejiang Sci-Tech University (11432932611902 and 11432932612014) as well as by a grant of CCCDI - UEFISCDI, project number PN-III-CEI-BIM-PBE-2020-0042 / 8 BM / 2021, and by Ministère de l'Education et de la Recherche de Roumanie and WBI.

References

1. A. R. Craze, M. M. Bhadbhade, Y. Komatsumaru, C. E. Marjo, S. Hayami and F. Li, *Inorg. Chem.*, 2020, **59**, 1274-1283.
2. S.-i. Ohkoshi, S. Takano, K. Imoto, M. Yoshikiyo, A. Namai and H. Tokoro, *Nature Photonics*, 2014, **8**, 65-71.
3. P. Gütlich, Y. Garcia and H. Spiering, in *Magnetism: Molecules to Materials IV: Nanosized Magnetic Materials*, ed. M. D. Joel S. Miller, Wiley-VCH Verlag GmbH & Co. KGaA, 2003, ch. 8, pp. 271-344.
4. P. Gütlich and H. A. Goodwin, *Topics in Current Chemistry. Spin Crossover in Transition Metal Compounds III.*, Springer-Verlag, Berlin, 2004.
5. S.-i. Ohkoshi, K. Imoto, Y. Tsunobuchi, S. Takano and H. Tokoro, *Nat. Chem.*, 2011, **3**, 564-569.
6. G. Molnár, S. Rat, L. Salmon, W. Nicolazzi and A. Bousseksou, *Adv. Mater.*, 2017, **30**, 1703862.
7. Y.-S. Meng and T. Liu, *Acc. Chem. Res.*, 2019, **52**, 1369-1379.
8. F.-J. Valverde-Muñoz, M. Seredyuk, M. C. Muñoz, G. Molnár, Y. S. Bibik and J. A. Real, *Angew. Chem., Int. Ed.*, 2020, **59**, 18632-18638.
9. M. A. Halcrow, *Chem. Soc. Rev.*, 2011, **40**, 4119-4142.
10. M. A. Halcrow, *Structure: Function Relationships in Molecular Spin-Crossover Materials*, Wiley & Sons, Chichester, 2013.
11. R. W. Hogue, S. Singh and S. Brooker, *Chem. Soc. Rev.*, 2018, **47**, 7303-7338.
12. S.-G. Wu, M. N. Hoque, J.-Y. Zheng, G.-Z. Huang, N. V. H. Anh, L. Ungur, W.-X. Zhang, Z.-P. Ni and M.-L. Tong, *CCS Chem.*, 2021, **3**, 453-459.
13. Z.-P. Ni, J.-L. Liu, M. N. Hoque, W. Liu, J.-Y. Li, Y.-C. Chen and M.-L. Tong, *Coord. Chem. Rev.*, 2017, **335**, 28-43.
14. F.-X. Shen, Q. Pi, L. Shi, D. Shao, H.-Q. Li, Y.-C. Sun and X.-Y. Wang, *Dalton Trans.*, 2019, **48**, 8815-8825.
15. A. R. Craze, H. Zenno, M. C. Pfrunder, J. C. McMurtrie, S. Hayami, J. K. Clegg and F. Li, *Inorg. Chem.*, 2021, **60,**, 6731-6738.
16. A. R. Zuluaga, A. J. Brock, M. C. Pfrunder, W. Phonsri, K. S. Murray, P. Harding, A. S. Micallef, K. M. Mullen, J. K. Clegg, D. J. Harding and J. C. McMurtrie, *Chem. Mater.*, 2020, **32**, 10076–10083.
17. A. B. Gaspar and M. Seredyuk, *Coord. Chem. Rev.*, 2014, **268**, 41-58.
18. M. Seredyuk, M. Carmen Munoz, V. Ksenofontov, P. Gütlich, Y. Galyametdinov and J. A. Real, *Inorg. Chem.*, 2014, **53**, 8442-8454.

19. I. Galadzhun, R. Kulmaczewski, O. Cespedes, M. Yamada, N. Yoshinari, T. Konno and M. A. Halcrow, *Inorg. Chem.*, 2018, **57**, 13761-13771.
20. R. Akiyoshi, R. Ohtani, L. F. Lindoy and S. Hayami, *Dalton Trans.*, 2021, **50**, 5065-5079.
21. H. L. C. Feltham, C. Johnson, A. B. S. Elliott, K. C. Gordon, M. Albrecht and S. Brooker, *Inorg. Chem.*, 2015, **54**, 2902-2909.
22. A. Kashiro, W. Kohno and T. Ishida, *Inorg. Chem.*, 2020, **59** 10163–10171.
23. B. L. Geoghegan, W. Phonsri, P. N. Horton, J. B. Orton, S. J. Coles, K. S. Murray, P. J. Cragg, M. K. Dymond and I. A. Gass, *Dalton Trans.*, 2019, **48**, 17340-17348.
24. T. Romero-Morcillo, M. Seredyuk, M. C. Muñoz and J. A. Real, *Angew. Chem., Int. Ed.*, 2015, **54**, 14777-14781.
25. J. A. Real, M. C. Muñoz, J. Faus and X. Solans, *Inorg. Chem.*, 1997, **36**, 3008-3013.
26. A. Galet, A. B. Gaspar, G. Agusti, M. C. Muñoz, G. Levchenko and J. A. Real, *Eur. J. Inorg. Chem.*, 2006, **2006**, 3571-3573.
27. A. L. Thompson, A. E. Goeta, J. A. Real, A. Galet and M. C. Muñoz, *Chem. Commun.*, 2004, 1390-1391.
28. H. Naggert, A. Bannwarth, S. Chemnitz, T. von Hofe, E. Quandt and F. Tuczek, *Dalton Trans.*, 2011, **40**, 6364-6366.
29. A. Pronschinske, R. C. Bruce, G. Lewis, Y. Chen, A. Calzolari, M. Buongiorno-Nardelli, D. A. Shultz, W. You and D. B. Dougherty, *Chem. Commun.*, 2013, **49**, 10446-10452.
30. H. Naggert, J. Rudnik, L. Kipgen, M. Bernien, F. Nickel, L. M. Arruda, W. Kuch, C. Näther and F. Tuczek, *J. Mater. Chem. C*, 2015, **3**, 7870-7877.
31. K. S. Kumar, M. Studniarek, B. Heinrich, J. Arabski, G. Schmerber, M. Bowen, S. Boukari, E. Beaurepaire, J. Dreiser and M. Ruben, *Adv. Mater.*, 2018, **30**, 1705416.
32. Z. Xin, T. N. D. Alpha, J. Xuanyuan, Z. Xiaozhe, Y. Yuewei, C. Xuegang, H. Xia, X. Xiaoshan and A. D. Peter, *Chem. Commun.*, 2018, **54**, 944-947.
33. Y.-H. Luo, Q.-L. Liu, L.-J. Yang, Y. Sun, J.-W. Wang, C.-Q. You and B.-W. Sun, *J. Mater. Chem. C*, 2016, **4**, 8061-8069.
34. Y.-H. Luo, M. Nihei, G.-J. Wen, B.-W. Sun and H. Oshio, *Inorg. Chem.*, 2016, **55**, 8147-8152.
35. S. Xue, Y. Guo, A. Rotaru, H. Müller-Bunz, G. G. Morgan, E. Trzop, E. Collet, J. Oláh and Y. Garcia, *Inorg. Chem.*, 2018, **57**, 9880-9891.
36. S. Ossinger, L. Kipgen, H. Naggert, M. Bernien, A. J. Britton, F. Nickel, L. M. Arruda, I. Kumberg, T. A. Engesser, E. Golias, C. Naether, F. Tuczek and W. Kuch, *J. Phys.: Condens. Matter*, 2020, **32**, 114003.
37. S. Ossinger, C. Nather and F. Tuczek, *J. Phys.: Condens. Matter*, 2020, **32**, 12.
38. S. Ossinger, C. Nather, A. Buchholz, M. Schmidtmann, S. Mangelsen, R. Beckhaus, W. Plass and F. Tuczek, *Inorg. Chem.*, 2020, **59**, 7966-7979.
39. S. Xue, A. Rotaru and Y. Garcia, *Hyperfine Interact.*, 2019, **240**, 91.
40. D. Pucci, G. Barberio, A. Crispini, M. Ghedini and O. Francescangeli, *Mol. Cryst. Liq. Cryst.*, 2003, **395**, 325-335.
41. K. Keisers, H. M. Hüppe, L. Iffland-Mühlhaus, A. Hoffmann, C. Göbel, U.-P. Apfel, B. Weber and S. Herres-Pawlis, *Inorg. Chem.*, 2020, **59**, 15343-15354.
42. G. Sheldrick, *Acta Crystallogr., Sect. A*, 2008, **64**, 112-122.
43. M. Llunell, D. Casanova, J. Cirera, P. Alemany and S. Alvarez, *SHAPE, Version 2.1*, Universitat de Barcelona, 2013.
44. O. Kahn, *Molecular Magnetism*, Wiley-VCH, New York, 1993.

Auxiliary alkyl chain modulated spin crossover behaviour in $[Fe(H_2Bpz_2)_2(C_n\text{-bipy})]$ complexes

Yunnan Guo[a,b], Aurelian Rotaru[c], Helge Müller-Bunz[d], Grace G. Morgan[d], Shishen Zhang[a], Shufang Xue[*,a,b] and Yann Garcia[*,b]

Table S1 Selected bond lengths (Å), angles (°) and structural parameters for **4** and **5**

4			**5**		
	100	293		100	130
Fe1-N2	2.0146(13)	2.1952(18)	Fe1-N1	1.998(2)	2.1432(13)
Fe1-N4	1.9926(13)	2.1374(17)	Fe1-N3	2.020(2)	2.1976(13)
Fe1-N6	2.0152(13)	2.2067(18)	Fe1-N5	2.024(2)	2.1856(13)
Fe1-N8	1.9985(14)	2.1391(17)	Fe1-N7	1.998(2)	2.1443(12)
Fe1-N9	1.9746(13)	2.2293(16)	Fe1-N9	1.977(2)	2.2220(12)
Fe1-N10	1.9705(13)	2.2260(16)	Fe1-N10	1.982(2)	2.2439(12)
$Fe\text{-}N_{av(pz)}$	2.0052(13)	2.1696(17)	$Fe\text{-}N_{av(pz)}$	2.010(2)	2.1678(12)
$Fe\text{-}N_{av(bipy)}$	1.9726(13)	2.2277(16)	$Fe\text{-}N_{av(bipy)}$	1.9795(2)	2.2330(12)
N2-Fe1-N4	88.82(5)	87.56(7)	N1-Fe1-N3	88.53(10)	86.45(5)
N2-Fe1-N6	175.90(5)	177.95(7)	N1-Fe1-N5	88.35(10)	90.09(5)
N2-Fe1-N8	88.82(5)	92.68(7)	N1-Fe1-N7	88.19(10)	96.66(5)
N2-Fe1-N9	95.17(5)	94.04(6)	N1-Fe1-N9	95.94(10)	97.98(5)
N2-Fe1-N10	86.25(5)	84.87(6)	N1-Fe1-N10	176.12(10)	168.73(5)
N4-Fe1-N6	88.05(5)	90.81(7)	N3-Fe1-N5	176.07(10)	176.41(5)
N4-Fe1-N8	88.46(5)	97.63(7)	N3-Fe1-N7	87.85(10)	90.80(5)
N4-Fe1-N9	94.99(5)	94.72(7)	N3-Fe1-N9	96.45(10)	96.86(4)
N4-Fe1-N10	173.63(5)	164.73(6)	N3-Fe1-N10	89.01(10)	88.10(4)
N6-Fe1-N8	88.44(5)	86.29(7)	N5-Fe1-N7	89.66(10)	88.65(5)
N6-Fe1-N9	87.75(5)	87.34(6)	N5-Fe1-N9	86.26(10)	84.56(5)
N6-Fe1-N10	97.06(5)	97.00(6)	N5-Fe1-N10	94.23(10)	95.47(5)
N8-Fe1-N9	174.77(5)	166.17(6)	N7-Fe1-N9	174.09(10)	163.85(5)
N8-Fe1-N10	95.46(5)	95.96(6)	N7-Fe1-N10	94.72(10)	93.27(5)
N9-Fe1-N10	81.46(5)	72.66(6)	N9-Fe1-N10	81.35(10)	72.88(4)
CShMs[a]	7.452	7.944	CShMs[a]	7.973	8.843
Σ[b]	44.63	64.12	Σ[b]	42.14	60.49

[a] CShMs: continuous shape measure values. [b] Σ is the sum of the deviation from 90° of the 12 *cis* angles of the FeN_6 octahedron.

Table S2. Supramolecular interaction involving C-H···O, π···π stacking interactions as well as C-H···π interactions for **4** and **5**

Type	Complex	D-H···A (Å)	H···A(Å)	D···A (Å)	D-H···A(◦)	Symmetry code
C-H···O	**4**	C2-H2···O2	2.6688(12)	3.5305(2)	151.02(10)	*x*, -*y*, -0.5+*z*
		C33-H33A···O3	2.5532(26)	3.3023(15)	146.78(92)	-*x*, *y*, 0.5-*z*
	5	C8-H8···O1	2.6967(22)	3.5762(4)	157.99(20)	*x*, 1-*y*, 0.5+*z*
		C33-H33A···O3	2.5532(26)	3.3561(4)	140.34(20)	1-*x*, 1-*y*, 2-*z*
π···π stacking (Type A)		Centre···Centre (Å)				
	4	3.347				
	5	3.330				
C-H···π (Type B)		C-H···Centre (Å)				
	4	3.348				
	5	3.338				

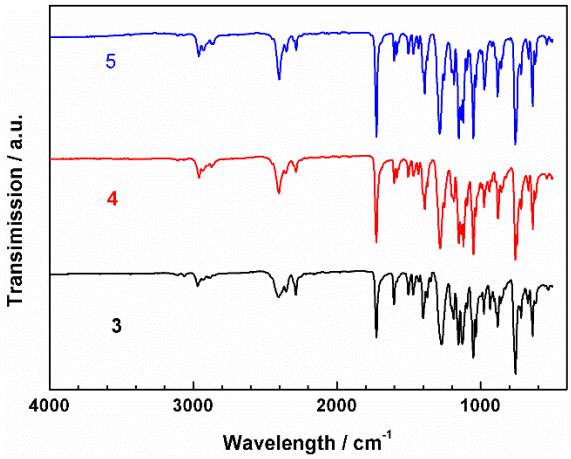

Fig. S1 IR spectra of powdered samples **3**-**5**.

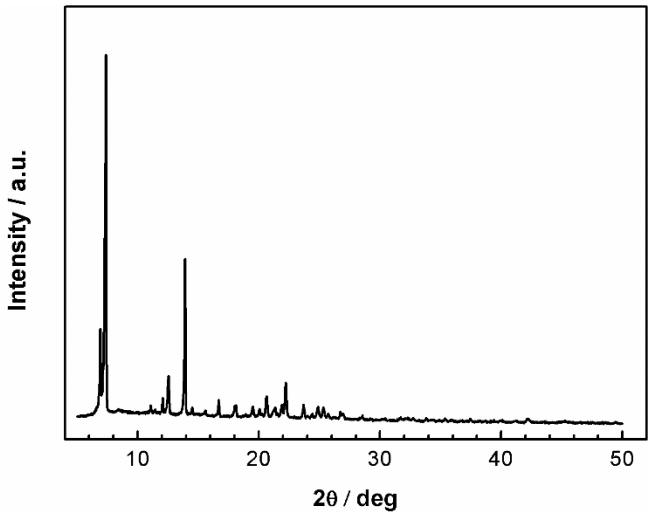

Fig. S2 X-ray powder diffraction patterns at 298 K for **3**.

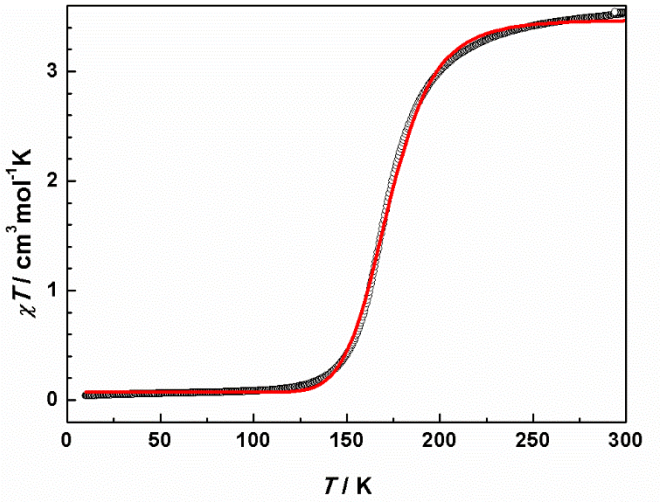

Fig. S3 Temperature-dependent $\chi_M T$ plots for **4**. The red solid curve corresponds to data fitting using the ideal solution model.[1]

Reference :

[1] O. Kahn. Molecular Magnetism, Wiley-VCH, New York, 1993.